On the Bandwidth and Beam Profile Characteristics of a Simple Low-Frequency Collimated Ultrasound Beam Source

J. Greenhall
Los Alamos National Laboratory,
P.O. Box 1663,
Los Alamos, NM 87545
e-mail: jgreenhall@lanl.gov

V. K. Chillara
Los Alamos National Laboratory,
P.O. Box 1663,
Los Alamos, NM 87545
e-mail: vchillara@lanl.gov

D. N. Sinha
Los Alamos National Laboratory,
P.O. Box 1663,
Los Alamos, NM 87545
e-mail: sinha@lanl.gov

C. Pantea
Los Alamos National Laboratory,
P.O. Box 1663,
Los Alamos, NM 87545
e-mail: pantea@lanl.gov

We numerically investigate the bandwidth and collimation characteristics of ultrasound beams generated by a simple collimated ultrasound beam source that consists of a piezoelectric disk operated near its radial mode resonances. We simulate the ultrasound beam generated in a fluid medium as a function of the excitation frequency for two cases: (1) free piezoelectric disk that corresponds to zero-traction along the lateral edge and (2) fixed piezoelectric disk that corresponds to zero-displacement along the lateral edge. We present and discuss the physical mechanism underpinning the frequency-dependent collimation and bandwidth properties of the ultrasound beams. We observe that the collimated beam generated by the free disk repeatedly lengthens/shortens and also extends/retracts sidelobes with increasing frequency. Alternatively, fixing the piezoelectric disk results in a consistent beam profile shape across a broad range of frequencies. This facilitates generating broadband signals such as a Gaussian pulse or chirp, which are common in ultrasound imaging. Thus, the fixed piezoelectric disk finds application as a collimated ultrasound beam source in a wide range of applications including medical ultrasound imaging, scanning acoustic microscopy, sonar detection, and other nondestructive ultrasound inspection techniques.
[DOI: 10.1115/1.4050851]

Keywords: acoustic emission, propagation and radiation, sensors and actuators

Contributed by the Noise Control and Acoustics Division of ASME for publication in the Journal of Vibration and Acoustics. Manuscript received January 2, 2020; final manuscript received March 31, 2021; published online May 4, 2021. Editor: Christopher D. Rahn.

1 Introduction

Collimated beams are attractive to the optics and acoustics communities because they are able to propagate long distances with little diffraction and demonstrate focusing regions that are significantly larger than traditional beams [1]. Collimated beams have the potential to benefit a range of acoustic applications including nano- and micro-particle manipulation [2,3] and acoustic imaging [4], where the narrow beamwidth improves lateral resolution and the large focusing region reduces spherical aberrations in the image. In practice, perfect collimation is not feasible due to diffraction, which causes the beam to spread radially as the beam propagates axially [5]. Thus, collimated beams have a finite width and length. Two common approaches to achieving collimation are generating beams with Gaussian or Bessel profiles [6]. Gaussian beams consist of a single central intensity peak that propagates with a constant width for a short period before expanding and decaying in amplitude. Alternatively, a Bessel beam experiences significantly less diffraction as it propagates, but it consists of multiple concentric intensity peaks surrounding the central beam. Collimated ultrasound beams have been studied theoretically [1] and demonstrated experimentally [7–13]. Typically, such ultrasound beams are generated using specifically designed piezoelectric disks. The first design consisted of annular patterned electrodes with each annular region excited individually with amplitudes and phases approximating a Bessel function [7,8]. More recently, Bessel beams have been generated using a three-dimensional (3D) printed axisymmetric grating [9] or a coiled-up-space metasurface to deflect incident acoustic waves toward a central collimated beam [10]. However, these techniques are limited due to the high degree of complexity required to fabricate and/or operate the transducers. Alternatively, Chillara et al. demonstrated a simple technique for generating a low-frequency collimated ultrasound beam (LF-CUB) by exciting the radial modes of a thin piezoelectric disk, which resulted in the generation of a beam with an approximately Bessel profile [12–14]. Additionally, it was found that clamping the lateral edges of the disk significantly reduces the amplitude of the Bessel-like side lobes at the radial mode frequencies, which narrowed the width and extended the length of the LF-CUB. This LF-CUB source has been investigated at discrete radial mode frequencies, but it has not been studied for its behavior at off-resonance frequencies. In contrast, many acoustic imaging techniques utilize broadband acoustic bursts [15,16]. Thus, the objective of this work is to analyze the broadband behavior of the LF-CUB source to determine the effective bandwidths and the corresponding beam profile characteristics that are important for practical implementation. To that end, we model the LF-CUB source numerically to (1) characterize the frequency-dependent surface vibration characteristics of the source with and without lateral constraint and (2) study the corresponding acoustic beam profile characteristics in water.

2 Simulation Setup

We analyze the axisymmetric behavior of the LF-CUB source using a frequency-dependent axisymmetric numerical solution in COMSOL [17]. The numerical model couples the mechanical and electrostatic interactions of the piezoelectric material [18] as well as the acoustic propagation in water [19]. Our LF-CUB source consists of a lead zirconate titanate (PZT-5A, Boston Piezo-Optics, Inc.) piezoelectric disk of radius $R = 25.0$ mm and thickness $h = 2.1$ mm submerged in water and excited by a sinusoidal voltage of amplitude V. We analyze the effects of "free" and "fixed" LF-CUB sources using zero-traction and zero-displacement boundary conditions on the radial edge ($r = R$), respectively.

3 Low-Frequency Collimated Ultrasound Beam Characterization

We characterize the beam profiles in terms of the nondimensionalized acoustic pressure $\bar{p} = p/\bar{T}_z \cdot 10^{-4}$, where $\bar{T}_z$ is the

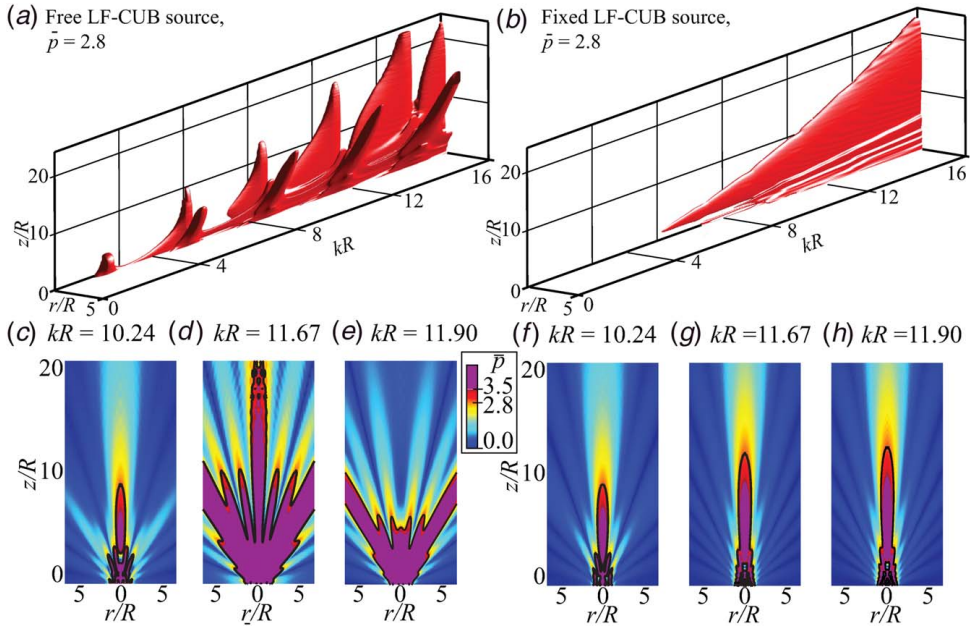

Fig. 1 Collimated ultrasound beam (CUB) profiles in the fluid for (*a*) free and (*b*) fixed LF-CUB sources. The beam profile is shown as an isosurface that represents the positions (*r*, *z*) and normalized frequency *kR* with constant nondimensionalized pressure $\bar{p} = 2.8$. Beam profiles are shown at three frequencies for (*c*)–(*e*) the free LF-CUB and (*f*)–(*h*) the fixed LF-CUB.

characteristic *z*-direction stress in the LF-CUB source for zero-strain and a stationary voltage *V* applied across the *z*-direction. Figure 1 shows the beam profiles in water for the free (Fig. 1(*a*)) and fixed LF-CUB source (Fig. 1(*b*)) as a function of normalized frequency $kR = 2\pi fR/c_{11}$, where c_{11} is the longitudinal sound speed in the LF-CUB source. In Fig. 1 the beam profiles are represented by isosurfaces that correspond to the positions (*r*, *z*) and normalized frequencies *kR* of constant pressure $\bar{p} = 2.8$. Here, we selected the isosurface threshold value $\bar{p} = 2.8$ arbitrarily to facilitate visualizing the beam profile trends of both the free and fixed LF-CUB sources. Additionally, we plot the beam profile cross-sectional pressure $\bar{p}$ of the free (Figs. 1(*c*)–1(*e*)) and fixed LF-CUB source (Figs. 1(*f*)–1(*h*)) excited at three selected frequencies. From Figs. 1(*a*) and 1(*c*)–1(*e*) we observe that the topology of the beam profile for the free LF-CUB source changes significantly with frequency. In between radial modes, the beam profile is dominated by the central beam (Fig. 1(*c*)), and increasing the frequency increases the beam length in the *z*-direction. When the frequency approaches a free radial mode (e.g., RM4, $kR = 11.79$), we observe a rapid growth of the central beam in the *z*-direction and growth of side lobes that extend rapidly with increasing frequency (Fig. 1(*d*)). As the frequency increases beyond the free radial mode, the central beam retracts rapidly briefly leaving only the side lobes (Fig. 1(*e*)) before they too retract. Subsequent increases in the frequency repeat the cycle of the slow growth of the central beam, rapid growth of the central beam and side lobes, and then retraction of the central beam and side lobes. Conversely, for the fixed LF-CUB source in Figs. 1(*b*) and 1(*f*)–1(*h*), we observe steady elongation of the central beam of the fixed LF-CUB source in the *z*-direction with increasing frequency. Near the fixed radial modes (e.g., RM3, $kR = 10.17$), we observe a slight elongation of the fixed LF-CUB source side lobes (Fig. 1(*f*)), but they are significantly less prominent than those of the free LF-CUB source at the same frequency (Fig. 1(*c*)).

To understand the mechanism behind the LF-CUB source behavior at different frequencies, we investigate the maximum surface displacement $|\xi_r|$ and $|\xi_z|$ in the *r*- and *z*-directions, respectively. Figure 2 shows the normalized surface displacement amplitude in the *r*-direction $\overline{\xi_r} = |\xi_r/\xi_{r0}|$ (solid) and *z*-direction $\overline{\xi_z} = |\xi_z/\xi_{z0}|$ (dashed) for the free (red/light) and fixed LF-CUB sources (black/dark). Here, ξ_{r0} and ξ_{z0} are the characteristic zero-stress displacements of the LF-CUB source in the *r*- and *z*-directions due to a constant voltage *V* across the *z*-direction. From Fig. 2, we observe a significant increase in the surface displacement amplitudes $\bar{\xi}_r$ and $\bar{\xi}_z$ of the free LF-CUB source (red/light) near the radial modes (Free RM1, Free RM2, Free RM3,…) of the free LF-CUB source, which approximately correspond to the zeros of a zero-order Bessel function $J_0(kR)$. For the free LF-CUB source $\bar{\xi}_r \approx \bar{\xi}_z$, which indicates the free LF-CUB source imparts a significant amount of energy into the fluid domain in the *r*-direction by developing side lobes, as demonstrated in Figs. 1(*a*) and 1(*c*)–1(*e*). For the fixed LF-CUB source, we observe that the *r*-displacement amplitude $\bar{\xi}_r$ increases at the radial modes of the fixed LF-CUB source, which approximately correspond to the zeros of a first-order Bessel function $J_1(kR)$. In contrast with the free LF-CUB source, the fixed LF-CUB source *z*-displacement amplitude $\bar{\xi}_z$ remains at an

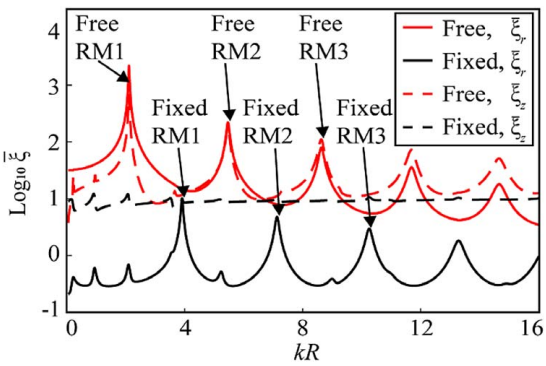

Fig. 2 CUB source surface displacement amplitudes $|\xi_r|$ and $|\xi_z|$ in the *r*- and *z*-directions, respectively, for the free and fixed LF-CUB sources with the radial modes (RM) indicated

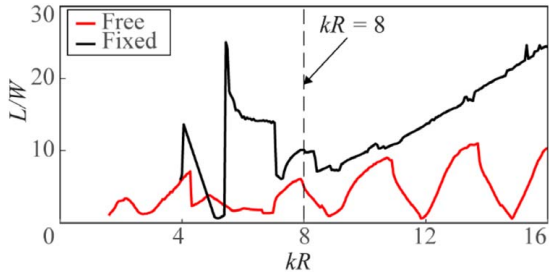

Fig. 3 Ratio between the beam length *L* and width *W* as a function of *kR* for the free and fixed collimated ultrasound beam sources and an ideal piston source

approximately constant value for all frequencies, where the value of $\bar{\xi}_z \geq \bar{\xi}_r$ at all frequencies and $\bar{\xi}_z \gg \bar{\xi}_r$ between fixed radial modes. As a result, the fixed LF-CUB source directs a larger portion of the acoustic energy in the z-direction of the fluid domain, which reduces the side lobes compared to the free LF-CUB source. We note that the surface displacement amplitudes $\bar{\xi}_r$ and $\bar{\xi}_z$ are larger for the free LF-CUB source than the fixed LF-CUB source. As a result, the maximum pressure amplitude generated in the fluid domain is higher for the free LF-CUB source than the fixed LF-CUB source.

In acoustic imaging, the achievable imaging depth and resolution are dependent on the z-depth penetration and lateral spread of the LF-CUB source. We quantify the z-depth penetration and lateral spread in terms of a beam length L and width W. Here, we define L and W as the furthest distance within the water for which $\bar{p}$ is above a specific threshold ($\bar{p} \geq 2.8$) in the r- and z-directions, respectively. We quantify the degree of collimation using the ratio L/W. Figure 3 shows the L/W ratio for the free (red/light) and fixed LF-CUB source (black/dark) and an ideal piston source (blue) as a function of frequency. For high frequencies ($kR \geq 8$), the fixed LF-CUB source L/W ratio increases quadratically with increasing frequency according to

$$L/W \approx 4.068(kR)^2 - 0.363(kR) - 1.1 \tag{1}$$

Conversely, for the free LF-CUB source we observe a periodic change in L/W with increasing frequency; with minima at the radial mode frequencies and maxima between radial mode frequencies. For frequencies $kR < 8$, the pressure generated by the LF-CUB source remains below the specified threshold ($\bar{p} < 2.8$) or it exceeds the threshold only in the nearfield region of the LF-CUB source, which results in L/W values that do not follow a readily identifiable trend. We note that different threshold values $\bar{p}$ still result in an L/W ratio that increases quadratically, but the quadratic coefficients are different. Thus, we demonstrate that fixing the lateral edges of the LF-CUB source by enforcing a zero-displacement constraint increases the L/W ratio, and thus improving the collimation of the LF-CUB. This is critical to acoustic imaging applications with broadband excitations because it ensures that the beam profile will remain narrow for the entire frequency range, as opposed to the free LF-CUB, whose profile varies greatly at different frequencies. In practice, a fixed LF-CUB source can be achieved by including an annular ring around the lateral edge of the piezoelectric disk. Real annular rings will not achieve the ideal zero-displacement boundary condition, but increasing annular ring material stiffness improves the approximation [13].

In conclusion, we have analyzed the frequency response of a LF-CUB that consists of a simple piezoelectric disk with either unsupported (free) or rigidly constrained lateral edges (fixed). We have modeled the LF-CUB source numerically using the Finite Element Method to account for piezoelectric, elastic, and acoustic interactions. Free LF-CUB source model results show a beam length-to-width ratio L/W that oscillates between minimum values at the radial mode frequencies and maximum values between the radial modes. Conversely, for the fixed LF-CUB source, we observe L/W that grows quadratically with frequency and is consistently larger than that of the free LF-CUB source. We attribute the increase in L/W of the fixed LF-CUB source to the fact that constraining the radial motion of the LF-CUB source redirects the energy to dissipate normally to the LF-CUB source in the z-direction of the fluid domain. Thus, we demonstrate that the fixed LF-CUB source increases L/W, thus providing enhanced and more consistent collimation over a wide range of frequencies, compared to the free LF-CUB source. This work provides insight into the LF-CUB source operation to facilitate maximizing the imaging distance and resolution of an ultrasound imaging system. As a result, this work finds application in medical ultrasound, scanning acoustic microscopy, sonar detection, and other nondestructive ultrasound inspection techniques.

Acknowledgment

This work was supported by the Laboratory Directed Research and Development Early Career Research program (Grant No. LDRD 20190568ECR) and by the U.S. Department of Energy, Office of Fossil Energy, Geologic Storage Technologies (Grant No. FE-855-817-FY17).

Conflict of Interest

There are no conflicts of interest.

Data Availability Statement

The authors attest that all data for this study are included in the paper. Data provided by a third party are listed in Acknowledgment.

References

[1] Durnin, J., Miceli, J. J., and Eberly, J. H., 1987, "Diffraction-Free Beams," Phys. Rev. Lett., **58**(15), pp. 1499–1501.
[2] Marston, P. L., 2006, "Axial Radiation Force of a Bessel Beam on a Sphere and Direction Reversal of the Force," J. Acoust. Soc. Am., **120**(6), pp. 3518–3524.
[3] Baudoin, M., and Thomas, J.-L., 2020, "Acoustic Tweezers for Particle and Fluid Micromanipulation," Annu. Rev. Fluid Mech., **52**(1), pp. 205–234.
[4] Lu, J.-, and Greenleaf, J. F., 1990, "Ultrasonic Nondiffracting Transducer for Medical Imaging," IEEE Trans. Ultrason. Eng., **37**(5), pp. 438–447.
[5] Milonni, P. W., and Eberly, J. H., 2010, *Laser Physics*, John Wiley & Sons Inc., Hoboken, NJ.
[6] Nowack, R. L., 2012, "A Tale of Two Beams: An Elementary Overview of Gaussian Beams and Bessel Beams," Stud. Geophys. Geod., **56**(2), pp. 355–372.
[7] Hsu, D. K., Margetan, F. J., and Thompson, D. O., 1989, "Bessel Beam Ultrasonic Transducer: Fabrication Method and Experimental Results," Appl. Phys. Lett., **55**(20), pp. 2066–2068.
[8] Campbell, J. A., and Soloway, S., 1990, "Generation of a Nondiffracting Beam With Frequency- Independent Beamwidth," J. Acoust. Soc. Am., **88**(5), pp. 2467–2477.
[9] Jimenez, N., Romero-Garcia, V., Pico, R., Cebrecos, A., Sanchez-Morcillo, V. J., Garcia-Raffi, L. M., Sanchez-Perez, J. V., and Staliunas, K., 2014, "Acoustic Bessel-Like Beam Formation by an Axisymmetric Grating," EPL, **106**(2), p. 24005.
[10] Li, Y., Liang, B., Gu, Z., Zou, X., and Cheng, J., 2013, "Reflected Wavefront Manipulation Based on Ultrathin Planar Acoustic Metasurfaces," Sci. Rep., **3**(1), p. 2546.
[11] Zhou, Q., Zhang, R., and Cao, W., 2019, "Elimination of Severe Near-Field Spatial Variations of Ultrasonic Transducers Using γ-Power Bessel Function Amplitude Distribution," Phys. Rev. App., **12**(3), p. 034056.
[12] Chillara, V. K., Pantea, C., and Sinha, D. N., 2017, "Low-Frequency Ultrasonic Bessel-Like Collimated Beam Generation From Radial Modes of Piezoelectric Transducers," Appl. Phys. Lett., **110**(6), p. 064101.
[13] Chillara, V. K., Pantea, C., and Sinha, D. N., 2018, "Radial Modes of Laterally Stiffened Piezoelectric Disc Transducers for Ultrasonic Collimated Beam Generation," Wave Motion, **76**, pp. 19–27.
[14] Chillara, V. K., Davis, E. S., Pantea, C., and Sinha, D. N., 2019, "Ultrasonic Bessel Beam Generation From Radial Modes of Piezoelectric Discs," Ultrasonics, **96**, pp. 140–148.

[15] Mamou, J., Aristizábal, O., Silverman, R. H., and Ketterling, J. A., 2008, "40-MHz Ultrasound Imaging with Chirps and Annular Arrays," Proceedings of the Annual International Conference of the IEEE Engineering in Medicine and Biology Society, Vancouver, British Columbia, Canada, Aug. 20–24, pp. 2518–2521.
[16] Maresca, D., Jansen, K., Renaud, G., van Soest, G., Li, X., Zhou, Q., de Jong, N., Shung, K. K., and van der Steen, A. F. W., 2012, "Intravascular Ultrasound Chirp Imaging," Appl. Phys. Lett., **100**(4), p. 043703.
[17] M, Jensen, H,2019, "Fine-Tuning the Design of Piezoelectric Transducers with Simulation," COMSOL Blog, https://www.comsol.com/blogs/fine-tuning-the-design-of-piezoelectric-transducers-with-simulation/.
[18] Tichý, J., Kittinger, E., Prívratská, J., and Erhart, J., 2010, *Fundamentals of Piezoelectric Sensorics: Mechanical, Dielectric, and Thermodynamical Properties of Piezoelectric Materials*, Springer Berlin/Heidelberg, Berlin, Heidelberg.
[19] Heywang, W., Lubitz, K., and Wersing, W., eds., 2008," *Piezoelectricity: Evolution and Future of a Technology*, Springer-Verlag, Berlin/Heidelberg.